AIAA JOURNAL
Vol. 45, No. 4, April 2007

Numerical Analysis of Airframe Noise Scattering Effects in Tilt-Rotor Systems

Damiano Casalino,* Mariano Genito,* and Antonio Visingardi*
Italian Aerospace Research Center (CIRA), 81043 Capua, Italy

DOI: 10.2514/1.24605

The present paper illustrates a computational aeroacoustic method for evaluating the effects of airframe scattering on the noise generated by a tilt-rotor system under realistic operating conditions. The physical model assumes ideal fluid, irrotational flow, and linear acoustic perturbation of the base flow. In a first step, the aerodynamic field about the rotating blades and the airframe is computed by solving a Laplace equation for the velocity potential, with vortical wakes shed from the blades and the wing, and freely convected in the field. In a second step, the unsteady pressure field on the blades is used to compute the noise signals around the prop rotor by means of an acoustic analogy approach. Then harmonic components are extracted from these signals and used to compute an equivalent source distribution in the prop-rotor region. In a third step, a convected wave equation for the acoustic velocity potential, with equivalent source terms, is solved in the frequency domain. This provides the tonal sound field generated by the prop rotor, propagating in the nonuniform flow past the airframe and reflected by structural components. In a final step, a Kirchhoff formulation is used to extrapolate the acoustic field past the aircraft in the far field, where the noise levels are compared to those generated by the same, but isolated prop rotor. As expected, significant scattering effects are observed at high blade passage frequencies.

Nomenclature

$\mathcal{B}, \mathcal{C}, \mathcal{D}$	=	BEM source influence coefficients
c	=	speed of sound
F_k	=	shape functions of wave equation
G	=	free-space Green's function
G^I_{nk}	=	pseudoinverse matrix element
i	=	imaginary unit, $\sqrt{-1}$
k	=	acoustic wave number, ω/c_∞
l	=	prop-rotor blade chord length
$\boldsymbol{n}$	=	outward normal unit vector
p	=	harmonic acoustic pressure
R_t	=	prop-rotor blade tip radius
$\boldsymbol{u}$	=	base flow velocity ($\boldsymbol{U} = \boldsymbol{u}/\boldsymbol{c}_\infty$)
$\boldsymbol{v}$	=	fluid velocity
α, σ, λ	=	PML damping factors
β	=	Prandtl–Glauert factor, $\sqrt{1 - M^2}$
γ	=	ratio of specific heats at constant pressure and volume
ρ	=	fluid density
Φ	=	velocity potential
ϕ'	=	acoustic velocity potential [$\phi = \mathrm{FT}(\phi')$]
ω	=	acoustic radian frequency

Subscripts

k	=	collocation node index
n	=	elementary source point index
∞	=	undisturbed medium properties

Presented as Paper 2608 at the 12th AIAA/CEAS Aeroacoustics Conference, Cambridge, MA, 8–10 May 2006; received 13 April 2006; revision received 13 November 2006; accepted for publication 29 November 2006.

*Research Engineer, Laboratory of Rotorcraft Aerodynamics and Aeroacoustics, via Maiorise.

I. Introduction

THE development of tilt-rotor aircraft plays a strategic role in the reduction of air traffic congestion at major airports. Because of their ability to operate in densely populated areas and to emulate short-to-medium range turboprop aircraft, tilt rotorcraft are a suitable candidate for future low-speed commuter transportation. Because the commercial competitiveness of a tilt rotor relies on its ability in meeting noise emission regulations, the reduction of noise levels must be considered from the earlier design stages. In this context, the employment of numerical tools for evaluating the noise sensitivity to several design parameters provides a viable alternative to expensive measurement campaigns.

The design of quiet rotorcraft and quiet landing/takeoff procedures strictly relies on the ability to simulate complex aeroacoustic mechanisms resulting from the interactions between the rotor, the vortical wakes, and the airframe under various operating conditions. In addition, the ability of a tilt rotorcraft to rotate the nacelle and to balance the lift between the rotor and the wing results in an increased number of possible operating conditions. As a consequence, the aerodynamic methods involved in the optimization processes must ensure a convenient compromise between physical reliability and computational efficiency.

Because of higher shaft speeds compared to helicopters, tilt rotors generate tonal noise peaks at higher frequencies. As a consequence, the presence of extended wing and tail components close to the prop rotor may have a significant influence on the far-field acoustic signature, thus the ability to evaluate the airframe scattering could play a crucial role in the optimization of noise shielding effects.

The numerical methodology illustrated in this paper is based on a simplified flow model in which the entropy is constant in the field (inviscid subsonic flow assumption), the vorticity is concentrated in thin layers shed from wing/blade edges and freely convected in the field (attached high-Reynolds-number flow assumption), and the acoustic fluctuation mode is coupled with the vortical fluctuation mode only via solid boundaries (silent vorticity assumption). In addition, the aerodynamic velocity field is supposed to be incompressible, with superposed linear acoustic perturbations. Under these assumptions, the solution of a Laplace equation for the velocity potential provides the aerodynamic field generated by the rotor/wake/airframe system [1], and the solution of a convected wave equation for the acoustic potential provides the acoustic field generated by the prop rotor and propagated in the nonuniform flow past the aircraft [2,3]. The matching between the unsteady

aerodynamic field past the prop rotor and the acoustic field is made by applying the acoustic analogy theory of aerodynamic sound [4,5]. The difference with respect to other full-scale aeroacoustic analyses carried out in recent years [6] lies in the method used to match a time-domain acoustic analogy computation for the isolated prop rotor with a frequency-domain acoustic field computation.

The main goal of the present work is to present a primary assessment of the Italian Aerospace Research Center (CIRA) comprehensive computational chain for rotorcraft aeroacoustic simulations. After a short illustration of the physical background of the aeroacoustic model in Sec. II, the aerodynamic and acoustic tools involved in the computational chain are described in Secs. III and IV. Demonstrative verification results are finally presented in Sec. V.

II. Physical Model

The aerodynamic field past a body immersed in an ideal and irrotational flow with uniform and steady conditions in the upstream far field is described by an equation for the velocity potential Φ that reads

$$c^2\nabla^2\Phi - \frac{\partial^2\Phi}{\partial t^2} - \frac{\partial v^2}{\partial t} - \nabla\Phi\cdot\nabla\left(\frac{v^2}{2}\right) = 0 \tag{1}$$

where $\mathbf{v} = \nabla\Phi$ is the fluid velocity and

$$c^2 = c_\infty^2 - (\gamma-1)\left(\frac{v^2 - v_\infty^2}{2}\right) - (\gamma-1)\frac{\partial\Phi}{\partial t} \tag{2}$$

is the local speed of sound. Substituting Eq. (2) into Eq. (1) the problem is restricted to the solution of a scalar nonlinear equation for the quantity Φ with appropriate boundary conditions.

When the problem under investigation involves a multibody system with parts in relative motion, such as a complete rotorcraft configuration, a computationally convenient practice is to further simplify the problem by assuming that the flow is incompressible. In this case Eq. (1) reduces to the Laplace equation $\nabla^2\Phi = 0$. This assumption is strictly valid in the limit of vanishing Mach and Helmholtz numbers. However, it can be reasonably used in the context illustrated earlier in this paper, if no shock waves appear in the aerodynamic field. Indeed, the unsteady pressure field on the surface of a body in a low-Mach-number vortical flow can be fairly well determined by considering only the solenoidal induction due to the field vorticity, provided that the vortex-body interactions generate acoustic waves of larger length compared to the body characteristic length. In the absence of significant blade-vortex interaction, as in forward flight conditions, the pressure fluctuations upon the blades of a rotorcraft are generated by the blade motion, by the variation of mean flow conditions at different azimuthal angles, and by the induction effect due to the wake shed from the trailing edge and washed away from the rotor. The corresponding chord-based Helmholtz number for the first rotor load harmonic is of order $\sim l/R_t$. This is sufficiently low to justify the present aerodynamic incompressible analysis.

The vorticity shed from the tip and trailing edges due to viscous effects can be taken into account into the Laplace flow model via an appropriate Kutta–Joukowski condition. The formulation used in the present work consists of assuming that the slip velocity jump at the trailing edge is supported by a vortex sheet across which the pressure is continuous and the potential is discontinuous. The potential jump $\Delta\Phi$ remains constant following any material point of the vortex sheet and equal to the value it had when the point left the edge.

The assumption of incompressible flow, even if reasonable for the calculation of the aerodynamic field, becomes unrealistic when the aim is to calculate the acoustic far field. A common practice in this case consists of assuming that the acoustic fluctuations are small-order perturbations of the base flow, which allows to linearize Eq. (1). Hence, by splitting the acoustic and the steady-base velocities, say $\boldsymbol{v}(\boldsymbol{x},t) = \boldsymbol{u}(\boldsymbol{x}) + \nabla\phi'(\boldsymbol{x},t)$ and $\nabla^2\Phi = \nabla\cdot\boldsymbol{u} + \nabla^2\phi'$, and by making use of the following linearization expressions:

$$v^2 \simeq u^2 + 2\boldsymbol{u}\cdot\nabla\phi' \tag{3}$$

$$c^2 \simeq c_\infty^2 - \frac{\gamma-1}{2}(u^2 - v_\infty^2) - (\gamma-1)\left(\frac{\partial\phi'}{\partial t} + \boldsymbol{u}\cdot\nabla\phi'\right) \tag{4}$$

Equation (1) takes the form of a linear wave equation that reads

$$c^2\nabla^2\phi' - \frac{\partial^2\phi}{\partial t^2} - 2\boldsymbol{u}\cdot\frac{\partial\nabla\phi'}{\partial t} - \boldsymbol{u}\cdot\nabla(\boldsymbol{u}\cdot\nabla\phi') - \nabla\left(\frac{v^2}{2}\right)\cdot\nabla\phi' - (\gamma-1)\left(\frac{\partial\phi'}{\partial t} + \boldsymbol{u}\cdot\nabla\phi'\right)\nabla\cdot\boldsymbol{u} = 0 \tag{5}$$

The linearity of Eq. (5) concurs to the possibility of a frequency-domain solution, with a benefit on the computational time required by the acoustic calculation. Using the $-i\omega t$ convention and the dimensionless flow velocity $\boldsymbol{U} = \boldsymbol{u}/\boldsymbol{c}_\infty$, the frequency-domain counterpart of Eq. (5) reads

$$\left[1 - \frac{\gamma-1}{2}(U^2 - U_\infty^2)\right]\frac{\partial^2\phi}{\partial x_i\partial x_i} - U_iU_j\frac{\partial^2\phi}{\partial x_i\partial x_j} + \left(i2kU_i - 2U_j\frac{\partial U_i}{\partial x_j} - (\gamma-1)\frac{\partial U_j}{\partial x_j}U_i\right)\frac{\partial\phi}{\partial x_i} + k\left(k + i(\gamma-1)\frac{\partial U_j}{\partial x_j}\right)\phi = 0 \tag{6}$$

where use of Einstein's convention of index summation has been made. Equation (6) describes the propagation of harmonic acoustic disturbances of velocity potential in a nonuniform irrotational steady flow. The corresponding acoustic pressure is provided by the accompanying linear expression

$$p = \rho_\infty c_\infty\left[1 - \frac{\gamma-1}{2}(U^2 - U_\infty^2)\right]^{\frac{1}{\gamma-1}}\left(ik\phi - U_i\frac{\partial\phi}{\partial x_i}\right) \tag{7}$$

Regarding the effect of vorticity on sound generation, it can be pointed out that in the present study the correct description of the tip-vortex dynamics is essential for the appropriate prediction of the blade pressure field. This provides, according to theory [5], the linear contribution to the aeroacoustic sources, which can be used to compute the noise from an isolated rotor via integral solutions of the Ffowcs–Williams and Hawkings (FW-H) equation, as proposed by Farassat and coworkers in many milestone papers [7–10]. In a shock-free aerodynamic field, the nonlinear contribution to the aeroacoustic sources depends only on the vortical fluctuations. However, this contribution can be neglected at the present Mach number ($\sim$0.2). Regarding the effect of vorticity on sound propagation, this is not taken into account by the present model, as the base flow is supposed to be irrotational, with vorticity concentrated in the wakes.

In the following sections the aerodynamic and acoustic numerical methods are presented, with emphasis placed on the method employed to extract the aeroacoustic sources from the unsteady aerodynamic field past the rotating blades, and to include them into the acoustic propagation model.

III. Aerodynamic Method

The aerodynamic code used in the present study is Rotorcraft Aerodynamic Modeling System (RAMSYS), which is an unsteady boundary element method (BEM) code for multibody configurations developed at CIRA [11], and based on Morino's boundary integral formulation [12]. In its incompressible functionality, RAMSYS solves the Laplace equation $\nabla^2\Phi = 0$ in a domain enclosed by the surface S, as depicted in Fig. 1. The surface S is composed of a surface S_b surrounding the body, a surface S_w surrounding the wake and a surface S_∞ in the far field. The boundary condition on S_b is the body impermeability, that is, $\partial\Phi/\partial n = \boldsymbol{v}_b\cdot\boldsymbol{n}$, where $\boldsymbol{v}_b$ is the kinematic velocity of a point on the body. The boundary condition on S_∞ is that of an undisturbed flow, that is, $\Phi = 0$.

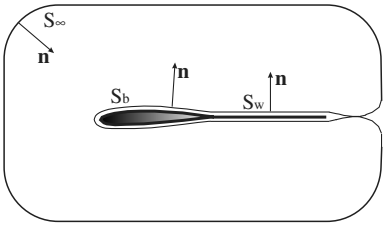

Fig. 1 Illustration of the aerodynamic domain.

The potential on the body can be determined by using the Green's function method through which the following integral expression of the Laplace equation can be obtained:

$$E(\boldsymbol{x}^\star)\Phi(\boldsymbol{x}^\star, t^\star) = \oint\!\!\!\!\!\!\int_{S_b} \left[G\frac{\partial \Phi}{\partial n} - \Phi\frac{\partial G}{\partial n} \right] \mathrm{d}S - \iint_{S_w} \Delta\Phi \frac{\partial G}{\partial n}\,\mathrm{d}S \tag{8}$$

where the two integrals at the right-hand side represent the contribution of the body and the wake, respectively; $E(\boldsymbol{x}^\star)$ is a domain function defined as zero outside S_b, $1/2$ on S_b and unity elsewhere; and $G = -1/4\pi|\boldsymbol{x} - \boldsymbol{x}^\star|$ is the free-space Green's function for the Laplace equation.

The body and wake surfaces are discretized by M and N hyperboloidal quadrilateral panels, respectively, on which the unknown potential is supposed to be constant (zeroth order). The main advantage of using these discretization elements is that the nodes of each panel are located on the body surface. In addition, as shown in [13], the analytical solution of surface integrals $\int G\,\mathrm{d}S$ and $\int(\partial G/\partial n)\,\mathrm{d}S$ arising from Eq. (8) is available. Using a collocation method with collocation points at the centroid of each element, the integral Eq. (8) yields an algebraic linear system of equations for the velocity potential Φ, that is,

$$E_k\Phi_k(t) = \sum_{m=1}^{M} \mathcal{B}_{km}\frac{\partial \Phi_m(t)}{\partial n} + \sum_{m=1}^{M} \mathcal{C}_{km}\Phi_m(t) + \sum_{n=1}^{N} \mathcal{D}_{kn}\Delta\Phi_n(t) \tag{9}$$

where the coefficients $\mathcal{B}_{km}$, $\mathcal{C}_{km}$ and $\mathcal{D}_{kn}$ account for the influence of equivalent body source, body doublet, and wake doublet distributions, respectively. The solution of the linear system (9) is finally solved by employing an iterative method of the Krylov family [14].

In Eq. (9) the value of $\Delta\Phi$ on each wake panel is obtained by using a Kutta–Joukowski hypothesis. The formulation adopted in RAMSYS [15,16] consists of requiring that no vortex filament exists at the trailing edge. This implies that the value of $\Delta\Phi$ across the wake and the body are equal at the trailing edge. This potential jump is computed by explicitly imposing that the pressure jump at the trailing edge is equal to zero. Hence, by making use of the generalized Bernoulli's equation, the Kutta–Joukowski condition results in the following nonlinear equation:

$$\Delta\left[\frac{\partial \Phi^{n+1}}{\partial t} + \boldsymbol{v}\cdot\nabla\Phi^{n+1} + \frac{1}{2}\nabla\Phi^{n}\cdot\nabla\Phi^{n+1} \right] = 0 \tag{10}$$

which is solved iteratively. Because the wake is modeled as a surface of discontinuity, which is not penetrated by the fluid and across which there is no pressure jump, $\Delta\Phi$ remains constant for each wake element, and equal to the value that the same element had when it left the trailing edge.

The convection path of each wake element is computed by using the instantaneous induced velocity at the wake nodes, due to the equivalent source distribution in Eq. (8). The application of the gradient operator to Eq. (8) yields the induced velocity at the generic point $\boldsymbol{x}^\star$:

$$\boldsymbol{v}(\boldsymbol{x}^\star, t^\star) = \oint\!\!\!\!\!\!\int_{S_b} \left[G\frac{\partial \Phi}{\partial n}\frac{\boldsymbol{x}-\boldsymbol{x}^\star}{|\boldsymbol{x}-\boldsymbol{x}^\star|^2} - \Phi\frac{\partial}{\partial n}\left(G\frac{\boldsymbol{x}-\boldsymbol{x}^\star}{|\boldsymbol{x}-\boldsymbol{x}^\star|^2} \right) \right] \mathrm{d}S - \iint_{S_w} \Delta\Phi\frac{\partial}{\partial n}\left(G\frac{\boldsymbol{x}-\boldsymbol{x}^\star}{|\boldsymbol{x}-\boldsymbol{x}^\star|^2} \right) \mathrm{d}S \tag{11}$$

IV. Aeroacoustic Method

A. Green's Function Discretization Scheme

The aeroacoustic code used in the present study is Green's function discretization (GFD) [17,18]. It solves Eq. (6) by using a wave-based finite-difference method for unstructured multi-element grids. As other wave-based methods, the discretization kernel is based on the use of approximate local solutions of the acoustic problem to build suitable shape functions for the unknowns and their derivatives. The shape functions in GFD are linear combinations of free-space Green's functions of the convected Helmholtz equation and their spatial derivatives. For instance, the second-order cross derivative $\phi_{x_1x_2}$ for a computational stencil of K nodes can be discretized as

$$\phi_{x_1x_2}(\boldsymbol{x}) = \sum_{k=1}^{K} F_k(\boldsymbol{x})\phi_k \tag{12}$$

where

$$F_k(\boldsymbol{x}) = \sum_{n=1}^{N} G^I_{nk} G_{x_1x_2}(\boldsymbol{x}, \boldsymbol{x}_n; \boldsymbol{M}) \tag{13}$$

are shape functions tailored to the frequency of the acoustic field, the local computational stencil, and the local mean flow velocity. The coefficients of the combination G^I_{nk} can be determined by seeking for an optimal intensity distribution of N fictitious sources upon a sphere surrounding the stencil. The discretized derivatives are used to convert the governing Eq. (6) and the boundary conditions into a sparse linear system that is solved by means of a sparse-matrix iterative method of the Krylov family [14].

The underlying properties of the GFD scheme and its accuracy have been addressed in previous studies, which show that the quality of the numerical solution is preserved up to 3–4 grid points per acoustic wavelength. Therefore in the following sections an error analysis is undertaken only for two novel features recently introduced in the code.

B. Perfect Matched Layer Boundary Conditions

The number of grid points in 3-D simulations dramatically increases with the extension of the computational domain. To contain both memory requirements and CPU time, suitable radiation conditions for boundaries placed relatively close to the acoustic sources are required. In [19] an approach based on a Dirichlet-to-Neumann mapping of the radiation boundary has been presented. This approach, when the inner integration surface surrounding the acoustic sources is placed in a region of relatively uniform flow, provides an "exact" radiation condition, regardless of the distance of the radiation boundary. The inconvenience of this approach lies in the additional CPU time required for evaluating two Kirchhoff integrals for each discretization element of the radiation boundary.

A more efficient approach has been used in the present work. This is based on a conventional perfect matched layer (PML) formulation for the convective Helmholtz equation, as also proposed in [20,21]. The basic idea of the PML method is to modify the wave equation in a layer close to the radiation boundary by introducing a dissipation term, whose effect is to transform an outgoing propagating wave into an outgoing evanescent wave, without spurious backward reflections. Consider, as a matter of convenience, a uniform flow parallel to the x_1 axis. Eliminating the mean flow gradients from Eq. (6), the wave equation takes the form

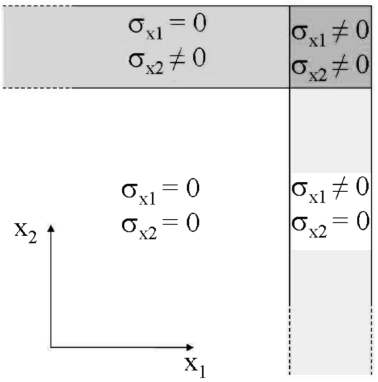

Fig. 2 Illustration of a computational domain with PML buffer layers.

$$\beta^2 \frac{\partial^2 \phi}{\partial x_1^2} + \frac{\partial^2 \phi}{\partial x_2^2} + \frac{\partial^2 \phi}{\partial x_3^2} + i2kM \frac{\partial \phi}{\partial x_1} + k^2 \phi = 0 \tag{14}$$

This can be converted into a Helmholtz equation $\nabla_\star^2 \phi^\star + k^2 \phi^\star = 0$ by using a Prandtl–Glauert transformation of the form

$$\phi(\boldsymbol{x}) = \phi^\star(\boldsymbol{x}) e^{-\frac{ikM}{\beta^2} x_1}, \qquad x_1^\star = \beta^2 x_1, \qquad x_2^\star = \beta x_2, \qquad x_3^\star = \beta x_3 \tag{15}$$

A PML layer for a wave propagating in the x_1 direction can be now obtained by introducing the so-called PML complex change of variable, say,

$$\frac{\partial}{\partial x_1^\star} \to \alpha(x_1^\star) \frac{\partial}{\partial x_1^\star}, \quad \text{with} \quad \alpha(x_1^\star) = \frac{1}{1 + i\sigma_1 / kc_\infty} \tag{16}$$

Finally, turning back to original variables, and considering a generic 3-D flow, the full set of PML transformations reads

$$\frac{\partial}{\partial x_i} \to \alpha_i(x_i) \frac{\partial}{\partial x_i} + i\lambda_i, \quad \text{with} \quad \alpha_i(x_i) = \frac{1}{1 + i\sigma_i / kc_\infty} \quad \text{and} \quad \lambda_i(x_i) = -\frac{kM_i}{\beta^2} \tag{17}$$

In the present work, the damping functions $\alpha_i(x_i)$ are supposed to be constant in the PML domain and are such that, as illustrated in Fig. 2, in a rectangular domain the fronts of the evanescent wave components are parallel to the radiation boundaries. The modified wave equation is thus obtained from Eq. (6) by substitution of

$$\frac{\partial \phi}{\partial x_i} \to \alpha_i \frac{\partial}{\partial x_i} + i\lambda_i \phi \tag{18}$$

$$\frac{\partial^2 \phi}{\partial x_i \partial x_j} \to \alpha_i \alpha_j \frac{\partial^2 \phi}{\partial x_i \partial x_j} + i\lambda_j \alpha_i \frac{\partial \phi}{\partial x_i} + i\lambda_i \alpha_j \frac{\partial \phi}{\partial x_j} - \lambda_i \lambda_j \phi \tag{19}$$

The PML treatment is completed with a condition for the external boundary where a common practice is to impose $\phi = 0$. In the present work the PML change of variables has been used to obtain the following modified Sommerfeld condition:

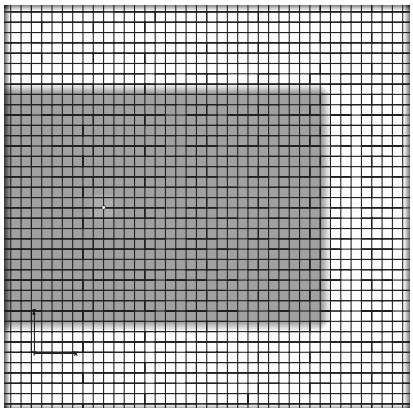

a) Computational domain

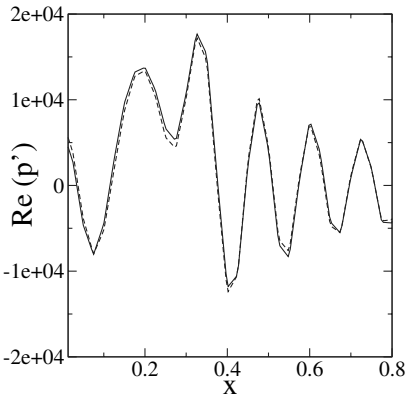

b) Acoustic pressure along the line $y = 0.5$, $z = 0.4$. ——: Numericalsolution, ----: analytical solution

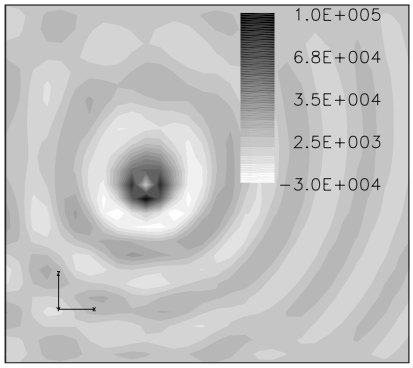

c) Analytical acoustic pressure field on the planey = 0.5. A zero value has been forced at the source location

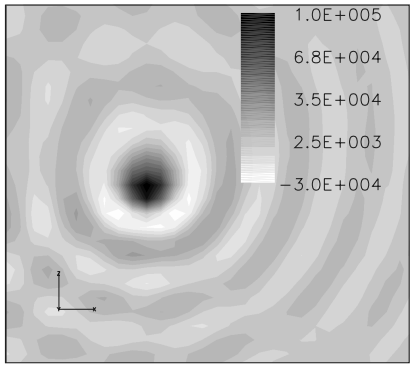

d) Numerical acoustic pressure field on the plane $y = 0.5$

Fig. 3 PML verification test case. The top-left figure illustrates the discretized computational domain, the source location, and the PML buffers. The other figures show the real part of the acoustic pressure for the case $\sigma/kc_\infty = 0.15$ and $M = (0, 0.2, 0.2)$.

$$\hat{n}_i\left(\alpha_i\frac{\partial\phi}{\partial x_i}+i\lambda_i\phi\right)-i\frac{k}{\beta^2}(\sqrt{M_n^2+\beta^2}-M_n)\phi=0 \qquad (20)$$

where M_n is the projection of the base flow Mach number in the outward normal direction $\hat{\boldsymbol{n}}$ to the boundary. This radiation condition is particularly convenient when the far-field boundary cuts a region of strong mean flow nonuniformity. In this case, in fact, instabilities may arise in the PML buffer due to the fact that, as pointed out in [22], the expression of the λ factor in Eq. (17) does not ensure a consistency in the phase and group velocities of the acoustic waves. Because a generalized space-time transformation that ensures stability is not available, a more robust approach consists of setting λ to zero and using, instead of a crude $\phi = 0$ condition, the modified Sommerfeld condition (20) that requires smaller values of the damping factor σ.

The accuracy of the PML treatment is now explored by considering the simple test case of a monopole source in a cubic domain, as illustrated in Fig. 3, for which the analytical solution is available. The cube has a unitary edge discretized with 41 points, the source location is (0.25, 0.5, 0.5), and the acoustic wave number is $k = 50$, corresponding to an average number of points per wavelength of about 3.7. A slip boundary condition is applied on the face $x = 0$, whereas a PML condition is applied on the other faces, with a layer thickness of 0.2. The mean flow is parallel to the wall ($M_1 = 0$) The L2-norm amplitude and phase errors with respect to the analytical solution are computed by considering only the numerical solution in the physical domain, which is represented in dark gray in Fig. 3a. A comparison between the numerical and the analytical solution is shown in Fig. 3b. Contours of $Re(p)$ are plotted in Figs. 3c and 3d for the analytical and numerical solution, respectively.

As a first test, the error dependence on the attenuation parameter σ/kc_∞ is checked in the absence of mean flow. The relative amplitude and phase L2-error are shown in Fig. 4a, where the curves obtained by solving Eq. (20) on the external boundaries are compared to those obtained by imposing $\phi = 0$. It is interesting to observe that, for values of the damping parameter higher than $\sim$0.15, the two formulations provide results of equivalent accuracy, whereas for lower values, the modified radiation condition yields better results. The value $\sigma/kc_\infty = 0.15$ is therefore used throughout this work, as the best candidate for more generic configurations. As a second test, the error dependence on the mean flow Mach number is checked. The corresponding error curves are plotted in Fig. 4b as a function of the two components (M_y, M_z). The curves exhibit a significant dependence on the Mach vector magnitude, and a less significant dependence on the flow direction. This can be explained by arguing that the number of grid points per wavelength is a function of the Mach number, and that the mean flow effects in the PML domain are properly accounted for by the $\boldsymbol{\lambda}$ vector in Eq. (17).

C. Source Synthesis Method

The peculiarity of the problem addressed in this study is that, because the noise sources are embedded in the propagation domain, they cannot be properly prescribed via boundary conditions. The main difficulty lies in the fact that the source region about the prop rotor must be permeable to waves scattered back by the airframe. A method has been thus developed, which enables the replacement of the prop rotor by a volume distribution of equivalent elementary sources. In a first step, the acoustic signals received by M microphones located on a closed mesh $\boldsymbol{y}_m$ around the isolated prop rotor are computed by using one of the several time-domain formulations proposed by Farassat and coworkers [7–10]. A discrete Fourier transform (FT) is then carried out to obtain the harmonic noise distribution $p(\boldsymbol{y}_m)$ at a prescribed frequency. In a second step, the complex magnitudes γ_n of a prescribed distribution of N monopole sources located at $\boldsymbol{x}_n$ nodes of the acoustic computation grid and enclosed by the microphone mesh are computed by inverting a linear system of the form

$$\sum_{n=1}^{N}[ikG(\boldsymbol{y}_m,\boldsymbol{x}_n;\boldsymbol{M})-\boldsymbol{M}\cdot G(\boldsymbol{y}_m,\boldsymbol{x}_n;\boldsymbol{M})]\gamma_n=\frac{p(\boldsymbol{y}_m)}{\rho_\infty c_\infty} \qquad (21)$$

where $\boldsymbol{M}$ denotes an averaged value of the mean flow Mach number in the equivalent source volume. In a final step, the monopole source distribution is used to build a right-hand side term of Eq. (6). Because a collocative discretization technique is used, the Dirac intensity of a monopole source at a grid node is spread upon its stencil by using a volume-energy-preserving 3-D Gaussian function of the form

$$\delta(d)=\frac{-3\log\epsilon}{4\pi D^3}\exp\left(\frac{d^3}{D^3}\log\epsilon\right) \qquad (22)$$

where d is the distance between the source point and a stencil node, D denotes a stencil reference length, and ϵ is the ratio between the value at a distance D and the bell peak at zero. The value $\epsilon = 10^{-7}$ has been used in the present study.

Infinite choices are now possible in setting the microphones/sources number and locations. The crucial point is the uniqueness of the acoustic field outside the microphone mesh. According to Kirchhoff theorem this is ensured by prescribing upon a closed surfaces around the sources both the pressure and its normal derivative. The equality of the normal derivative can be imposed by distributing the microphones upon a double-layer mesh. Moreover, numerical tests have shown that the best accuracy is ensured by distributing the sources upon a regular structured mesh constituted of two layers adjacent to the microphone mesh. The acoustic results presented in Sec. V have been obtained by using a cylindrical-extruded structured grid in the prop-rotor region, matched with an unstructured tetrahedral one in the rest of the computational domain. The microphone and the source grids are two coaxial double-layer annular cylinders extracted from the

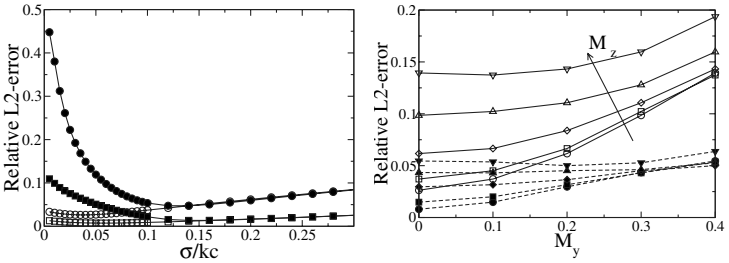

a) Test 1: effect of the damping coefficient. ○: amplitude error, □: phase error. Filled and empty symbols denote errors obtained by imposing $\phi = 0$ and Eq. (20) on the external boundary, respectively

b) Test 2: effect of the mean flow. ——: amplitude error, ----: phase error. Symbols denote different values of M_z in the interval [0,0.4]

Fig. 4 PML verification tests. Amplitude/phase L2-errors analysis.

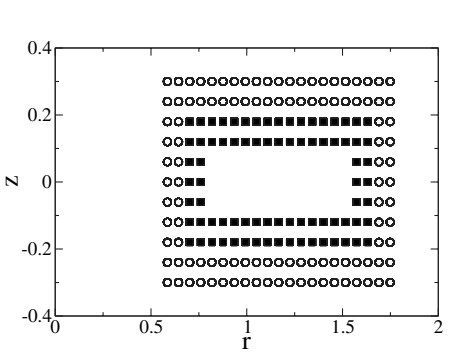

a) Microphone/source distribution in a plane parallel to the prop-rotor axis, and cutting through the rotation center. ○: microphones, □: equivalent sources

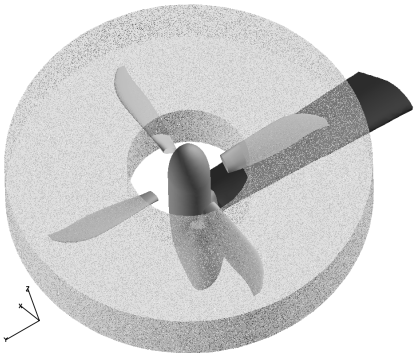

b) Annular microphone mesh around the prop rotor

Fig. 5 Setup of the source synthesis method.

structured grid, as depicted in Fig. 5. The corresponding numbers of microphones and sources are $M = 13,440$ and $N = 9600$, and the underdetermined linear system (21) is solved by means of the parallel least-square iterative solver embedded in the GFD code, which ensures the best $L2$-norm fitting of the pressure field distribution upon the microphone surface.

The accuracy of the source synthesis method is addressed in Sec. V by using, as a reference solution, the noise computed by replacing the full structured volume around the prop rotor with a Dirichlet condition applied to its external boundary, and by eliminating any scattering component from the computational domain.

V. Numerical Analysis

In this section results of the tilt-rotor aeroacoustic analysis are presented. The configuration is one of those addressed in the European research project TILTAERO, and corresponds to a conversion flight condition, with the prop-rotor axis pivoted about 60 deg with respect to the freestream and the wing chord. Parts of the aerodynamic results necessary to the present analysis have been obtained in the TILTAERO context, where the RAMSYS results have been checked against Euler and Navier–Stokes results [23]. Only a subset of these aerodynamic results is herein reported, the emphasis being placed on the novel acoustic results.

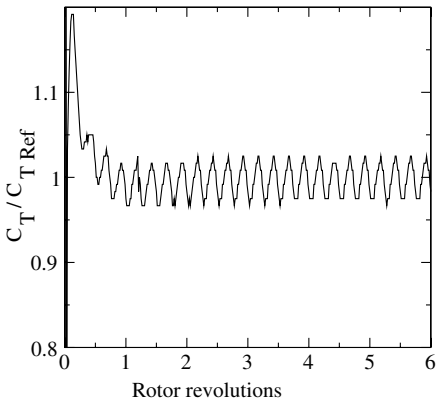

a) Convergence history of the prop-rotor thrust coefficient

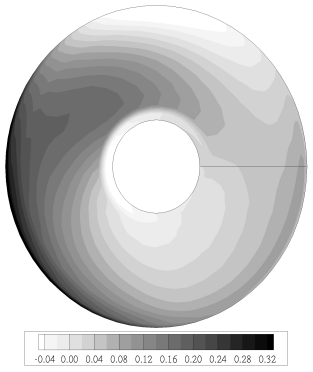

b) Normal force distribution along the blade span and at different azimuthal locations

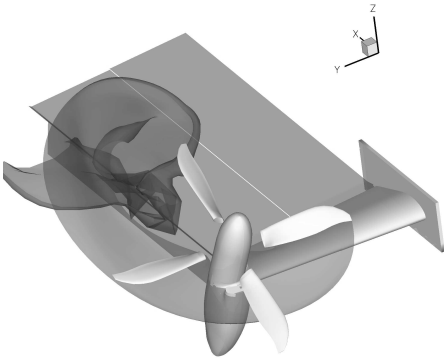

c) Blade/wing wake interaction. For clarity purposes, only one blade-wake is represented

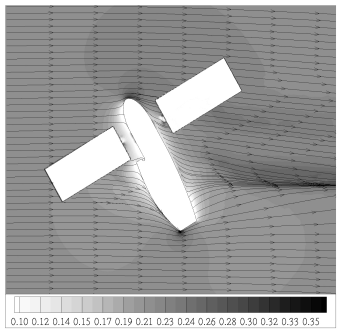

d) Mean flow Mach contours and streamlines. The clear areas denote the engine nacelle and the equivalent source region

Fig. 6 RAMSYS aerodynamic results.

The computational analysis is performed in three steps:

1) The unsteady aerodynamic field upon the prop-rotor blades and the wing is computed by running RAMSYS. The blade pressure field provides the input for the second step analysis, whereas the evaluation of the integral (11) in a postprocessing phase provides the unsteady velocity at each node of the acoustic computation grid. The steady velocity field required in the third step analysis is then obtained via a time average over a rotor-revolution period.

2) The pressure field on the blades is used by the FW-H code object-oriented library for aeroacoustics (OLA) [24] to generate the acoustic signals upon the surrounding microphone surface. The second and third blade passage frequency (BPF) spectral components are extracted from the signals and then used to compute equivalent source distributions.

3) The acoustic field generated by the equivalent sources, scattered by the airframe components and refracted by the steady off-rotor aerodynamic field is performed by running GFD in a domain-decomposition parallel modality. To highlight scattering effects due to both airframe and flow, the noise computed for the full rotorcraft system with flow is compared to that obtained in the absence of flow for both the full system and the isolated prop rotor.

A. Computational Setup

A box grid with a 10% PML thickness in each direction is discretized with about 1.7×10^6 nodes. A full unstructured tetrahedral grid is matched with an annular hexahedral mesh in the equivalent source region. Pyramidal volume elements are located at the interface between the structured and unstructured mesh. A slip boundary condition is applied to the plane $y = 0$, and a PML radiation condition on the other five faces. An inner control surface is inserted around the tilt-rotor system, upon which a Kirchhoff integral is performed to evaluate the acoustic far-field radiation. This is computed on rectangular domains $(-1.07\text{E}+01)R_t \leq x \leq (1.17\text{E}+01)R_t$ and $(8.46\text{E}-01)R_t \leq y \leq (1.00\text{E}+01)R_t$ on planes $z = \pm 7.31R_t$. Noise levels at a given frequency are represented in nondimensional form by using, as reference value, the maximum acoustic pressure at the same frequency on the surface that bounds the equivalent source region.

B. Aerodynamic Results

In the present configuration, the freestream is aligned with the x axis and has a magnitude of $M_\infty = 0.21$. The prop-rotor angular speed is such that the first BPF tonal noise peak corresponds to the Helmholtz number $kR_t = 25.5$.

The convergence and physical reliability of the RAMSYS computation is controlled by looking at the thrust coefficient, whose time-averaged value is close to the reference value precomputed in the blind test activity of the TILTAERO project [23], and whose fluctuating part, as shown in Fig. 6a, is stabilized after three rotor revolutions. The corresponding blade distribution of the normal force is plotted in Fig. 6b, in which the reverse-flow region is clearly visible at azimuthal blade locations close to 270 deg. The interaction between the wake shed from the wing and the wake from one of the four blades is shown in Fig. 6c. Finally, Fig. 6d shows the mean flow Mach contours and streamlines in a $y = \text{const}$ plane past the engine nacelle. Other details and results can be found in [23].

C. Isolated Prop-Rotor Acoustic Analysis

To use the aerodynamic output as input for an acoustic analysis in the frequency domain, a matching strategy has been developed and discussed in Sec. IV. This is based on the use of a FW-H acoustic analogy formulation to compute the noise signals upon a closed surface encompassing the prop rotor. The distance between the blades and the microphones is such that the density and pressure fluctuations are in the isentropic ratio, as required by the acoustic

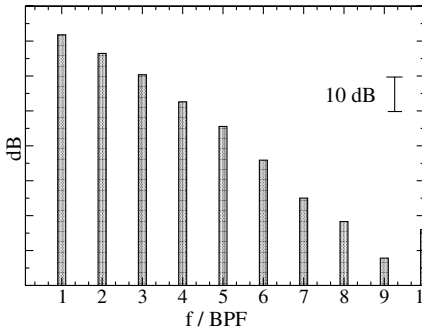

a) Narrowband noise spectrum (SPL) at a generic microphone location

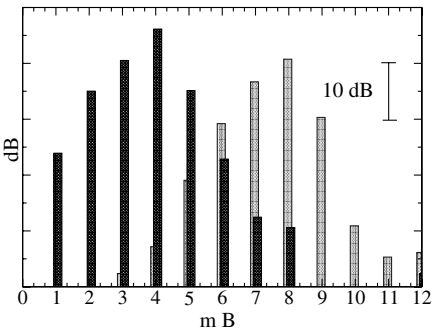

b) Noise levels (SPL) of 1st and 2nd BPF noise components at a given radial distance against the azimuthal mode order *m*. Dark gray: 1st BPF, bright gray 2nd BPF

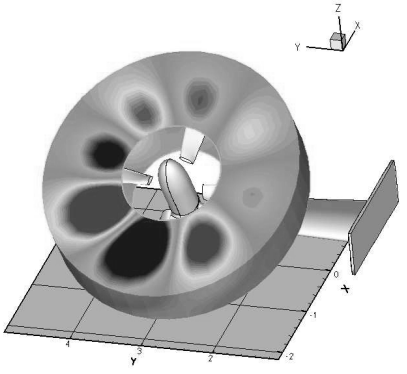

c) Real part of the 1st BPF component of the acoustic pressure

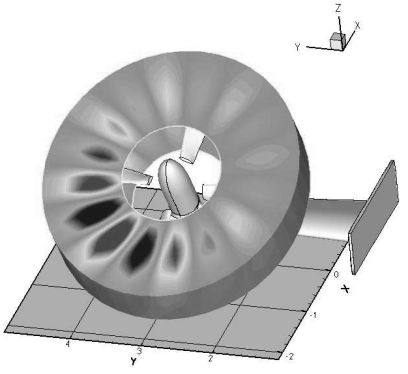

d) Real part of the 2nd BPF component of the acoustic pressure

Fig. 7 Analysis of the acoustic field generated by the prop rotor on the microphone surface.

analogy theory. The CIRA code OLA [24] is used for this task. Among various formulations available in OLA for both the subsonic and the supersonic regime, the well-known formulation 1A by Farassat [8] is used. Integrals are evaluated in time by means of a forward-time scheme. The employed microphone surface is shown in Fig. 5. It is constituted by two nested surfaces at a reciprocal distance of about $6.5 \times 10^{-2} R_t$. Such a small value ensures a good representation of the normal derivative of the acoustic pressure.

As expected for the present aeroacoustic simulation, the deterministic blade loading computed by RAMSYS generates a discrete frequency noise at harmonics of the BPF. This is shown in Fig. 7a, in which the narrowband spectrum of one of the 13,440 noise signals is plotted. The azimuthal structure of the acoustic field can be also analyzed by extracting the harmonic levels at a given radial distance and performing a spatial Fourier analysis. The results are illustrated in Fig. 7b, in which the harmonic peaks for the first and second BPF are plotted against the azimuthal mode order. As predicted by theory, the Doppler effect for a rotating device is such that the loading unsteadiness results in a spreading of the azimuthal radiation pattern around the modal order corresponding to the BPF order. In other words, the nth harmonic of the aerodynamic loading acting on one of the B blades of a rotor generates an acoustic field whose mth BPF levels have azimuthal order $mB \pm n$. As a further proof of theory, the first and second BPF level distributions on the microphone surface are shown in Figs. 7c and 7d, respectively.

The source extraction method has been developed and verified with simple model problems by computing the sound generated by moving elementary sources and radiated in a free field discretized with a regular Cartesian mesh. The source is introduced either via a Dirichlet condition applied to the boundary of a hole in the mesh that encompasses the sources, or via equivalent sources distributed on the nodes of a mesh that fills the same hole. The equality of the two numerical solution has been used as accuracy criterion in the verification process. In this paper, the same verification test is carried out, but for the actual prop-rotor configuration and the actual unstructured multi-element mesh, deprived of the wing/nacelle components and with radiation conditions applied on the six boundary faces of the computational domain. In this case, however, the two meshes are not strictly the same. In fact, the mesh used for the computation with Dirichlet boundary condition is obtained by suppressing the annular structured block shown in Fig. 5b. The resulting mesh is therefore a genuine tetrahedral mesh without pyramidal elements at the unstructured/structured matching surface. In spite of this significant difference, the far-field noise levels compare fairly well. This is shown in Fig. 8, in which the sound pressure contours on the plane $z = -7.31 R_t$ are plotted. The sound level difference between the Dirichlet solution p_1 and the equivalent source solution p_2 can be estimated by computing the quantity $\Delta\text{dB} = 10 \log(|\int |p_1|^2 \text{d}S - \int |p_2|^2 \text{d}S| / \int |p_1|^2 \text{d}S) = 4.1$ dB.

D. Tilt-Rotor Aeroacoustic Results

Two sets of aeroacoustic results are herein presented, corresponding to the second and third BPF prop-rotor tone noise. The first BPF harmonic is not addressed in this paper, because the effects of airframe scattering (body reflection and flow refraction) are expected to be less significant than at higher frequencies. The scattering effects are evaluated by comparing the near and far acoustic field generated by the isolated prop rotor in a medium at rest to that generated by the same prop rotor and scattered by the wing/nacelle components, both with and without mean flow.

Figure 9 shows results for the second BPF case. At a first look, the wave fronts are not remarkably affected by the airframe. This is because the dominant effect on sound propagation is due to the presence of a rigid surface at $y = 0$ that masks any other scattering effect. However, the far-field noise contours on a plane opposite to the wing pressure side show that 1) the far-field noise levels are enhanced by the airframe reflection (shielding effect) and 2) the flow has a significant influence on the noise levels and directivity pattern. Indeed the presence of the flow affects the effective mutual location of prop rotor and wing, resulting in a different reflection pattern.

Figure 10 shows results for the third BPF case. At this frequency, both the reflection and refraction phenomena can be clearly appreciated. In particular, the mechanisms of waves diffraction by the wind leading- and trailing-edge seem to be significantly affected by the presence of the flow, resulting in a different directivity pattern and higher noise levels. A deeper analysis is, however, necessary to better understand the reciprocal role of each mechanism involved in the problem.

E. CPU-Time Assessment

The RAMSYS run has required about 8 h on a NEC SX-6 vectorial supercomputer to compute both the unsteady pressure field on the blades and the velocity field at about 1.7×10^6 nodes in the volume

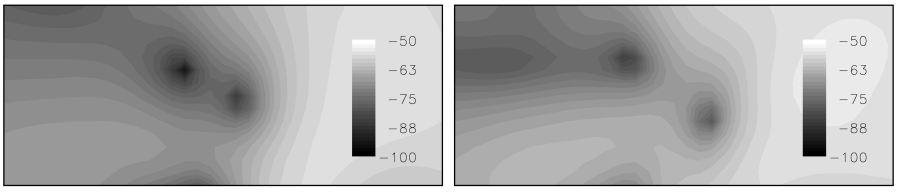

Fig. 8 Verification of the equivalent source method: comparison of the second BPF sound levels on the plane $z = -7.31 R_t$ obtained via a Dirichlet condition imposed around the prop rotor (left) and an equivalent source distribution (right).

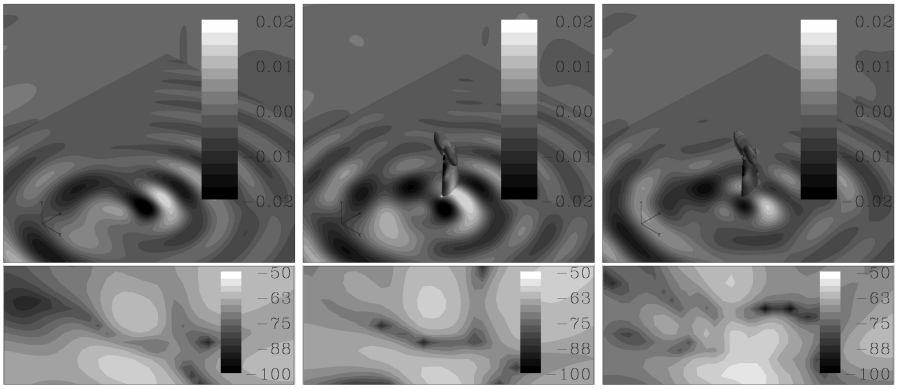

Fig. 9 Second BPF acoustic field: isolated rotor without flow (left), full system without flow (middle), full system with flow (right). In the top figures the nondimensional real part of the acoustic pressure is plotted, whereas the far-field sound pressure level contours at $z = 7.31 R_t$ are plotted on the bottom figures.

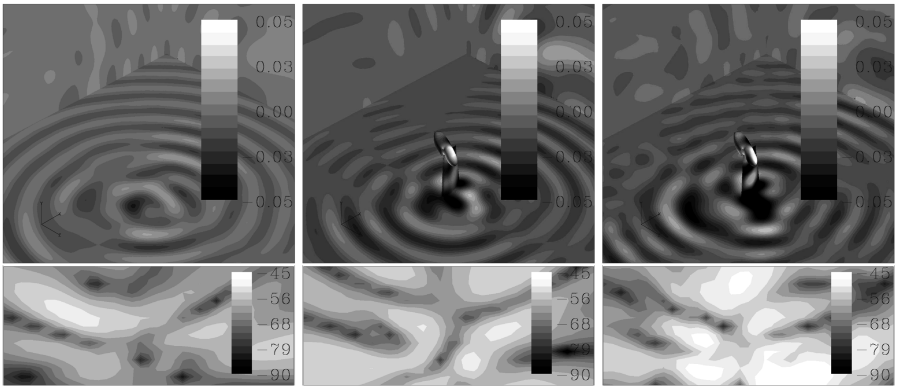

Fig. 10 Third BPF acoustic field: isolated rotor without flow (left), full system without flow (middle), full system with flow (right). In the top figures the nondimensional real part of the acoustic pressure is plotted, whereas the far-field sound pressure level contours at $z = 7.31R_t$ are plotted on the bottom figures.

past the rotorcraft. The OLA run has required about 2 h on a four-processor NEC TX-7 system to compute about 13,000 noise signals on the boundary of the equivalent source domain, generated during two prop-rotor revolutions. Finally, the GFD run has required about 12 h on a four-processor NEC TX-7 system to compute the acoustic field (potential, pressure, intensity vector field) at about 1.7×10^6 nodes in the volume past the rotorcraft.

VI. Conclusions

An aeroacoustic method based on a time-domain FW-H rotor acoustic analysis matched with a frequency-domain GFD field acoustic analysis has been presented. This is used to predict the acoustic propagation about a realistic tilt-rotor system in conversion flight conditions, by replacing the prop rotor with a distribution of equivalent elementary sources. A primary assessment of the BEM/FW-H/GFD computational chain has demonstrated its practical relevance for the improvement of airframe noise shielding effects. Unfortunately, due to the presence of a reflecting plane in the wing midspan section of the tilt-rotor system, effects due to the airframe reflection have been dramatically masked. In spite of the weak influence of the airframe reflection, a significant effect due to the flow has been observed. This demonstrates that, even at the present low Mach number, the solution of a Helmholtz problem to investigate the airframe scattering may yield unreliable results.

Acknowledgments

The authors wish to thank the Consortium of the European research project TILTAERO (Contract No. G4RD-CT-2001-00477) for authorizing the use of the tilt-rotor geometry and the precomputed trim conditions.

References

[1] Morino, L., *Computational Methods in Potential Aerodynamics*, Springer–Verlag, Berlin, 1986.

[2] Pierce, A. D., "Wave Equation for Sound in Fluids with Unsteady Inhomogeneous Flow," *Journal of the Acoustical Society of America*, Vol. 87, No. 6, 1990, pp. 2292–2299.

[3] Astley, R. J., and Bain, J. G., "A Three-Dimensional Boundary Element Scheme for Acoustic Radiation in Low Mach Number Flows," *Journal of Sound and Vibration*, Vol. 109, No. 3, 1986, pp. 445–465.

[4] Lighthill, M. J., "On Sound Generated Aerodynamically: 1. General Theory," *Proceedings of the Royal Society of London A*, Vol. A211, No. 11071952, pp. 564–578.

[5] Ffowcs Williams, J. E., and Hawkings, D. L., "Sound Generated by Turbulence and Surfaces in Arbitrary Motion," *Philosophical Transactions of the Royal Society of London, Series A: Mathematical and Physical Sciences*, Vol. A264, No. 1151, 1969, pp. 321–342.

[6] Stanescu, D., Hussaini, M. Y., and Farassat, F., "Large Scale Frequency Domain Numerical Simulation of Aircraft Engine Tone Noise Radiation and Scattering," AIAA Paper 2002-2586, 2002.

[7] Farassat, F., "Theory of Noise Generation from Moving Bodies with an Application to Helicopter Rotors," NASA Technical Report R-451, 1975.

[8] Farassat, F., and Succi, G. P., "The Prediction of Helicopter Discrete Frequency Noise," *Vertica*, Vol. 7, No. 4, 1983, pp. 309–320.

[9] Farassat, F., and Brentner, K. S., "The Uses and Abuses of the Acoustic Analogy in Helicopter Rotor Noise Prediction," *Journal of the American Helicopter Society*, Vol. 33, No. 1, 1988, pp. 29–36.

[10] Brentner, K. S., and Farassat, F., "Analytical Comparison of the Acoustic Analogy and Kirchhoff Formulation for Moving Surfaces," *AIAA Journal*, Vol. 36, No. 8, 1998, pp. 1379–1386.

[11] Visingardi, A., D'Alascio, A., Pagano, A., and Renzoni, P., "Validation of CIRA's Rotorcraft Aerodynamic Modelling SYSstem with DNW Experimental Data," *22nd European Rotorcraft Forum*, Paper 57, Brighton, U.K.,1996.

[12] Banerjee, P. K., and Morino, L., *Developments in Boundary Element Methods, Volume 6: Nonlinear Problems of Fluid Dynamics*, Elsevier Applied Science Publishers, Barking, U.K., 1990.

[13] Preuss, R., and Morino, L., "Evaluation of the Doublet for a Hyperboloidal Element," Energy Research and Development Administration, ENGR-CCMP-TN-76-04, Washington, DC, Nov. 1976.

[14] Saad, Y., and Schultz, M. H., "A Generalized Minimal Residual Algorithm for Solving Non Symmetric Linear Systems," *SIAM Journal on Scientific and Statistical Computing*, Vol. 7, No. 3, 1986, pp. 856–869.

[15] Kinnas, S. A., and Hsin, C. Y., "Boundary Element Method for the Analysis of the Unsteady Flow Around Extreme Propeller Geometries," *AIAA Journal*, Vol. 30, No. 3, 1992, pp. 688–696.

[16] D'Alascio, A., Visingardi, A., and Renzoni, P., "Explicit Kutta Condition Correction for Rotary Wing Flows," *19th World Conference on the Boundary Element Method*, Computational Mechanics Publications, Southampton, U.K., 1997, pp. 779–788.

[17] Di Francescantonio, P., and Casalino, D., "Green's Function Discretization Scheme for Sound Propagation in Nonuniform Flows," *AIAA Journal*, Vol. 37, No. 10, 1999, pp. 1161–1172.

[18] Casalino, D., Roger, M., and Jacob, M., "Prediction of Sound Propagation in Ducted Potential Flows Using Green's Function Discretization," *AIAA Journal*, Vol. 42, No. 4, 2004, pp. 736–744.

[19] Di Francescantonio, P., Casalino, D., and De Mercato, L., "Aeroacoustic Design of Aero-engine Intake Liners," AIAA Paper 2005-2942, May 2005.

[20] Hu, F. Q., "Absorbing Boundary Condition," *International Journal of Computational Fluid Dynamics*, Vol. 18, No. 6, 2004, pp. 513–522.

[21] Bécache, E., Dhia, A. S. B.-B., and Legendre, G., "Perfectly Matched Layers for the Convected Helmholtz Equation," *SIAM Journal on Numerical Analysis*, Vol. 42, No. 1, 2004, pp. 409–433.

[22] Hu, F. Q., "A Perfectly Matched Layer Absorbing Boundary Condition for Linearized Euler Equations with a Non-Uniform Mean Flow," *Journal of Computational Physics*, Vol. 208, No. 2, 2005, pp. 469–492.

[23] Visingardi, A., Decours, J., Khier, W., and Voutsinas, S., "Code-to-Code Comparisons for the Blind-Test Activity of the Tiltaero Project," *31st European Rotorcraft Forum*, Paper 73, Florence, Italy, 2005.

[24] Fitzpatrick, J. A., "Aeroacoustics Research in Europe: The CEAS-ASC Report on 2004 Highlights," *Journal of Sound and Vibration*, Vol. 288, Nos. 1–2, 2005, pp. 1–32.

Z. Wang
Associate Editor